IIETA International Information and Engineering Technology Association
Advancing the World of Information and Engineering

Mathematical Modelling of Engineering Problems
Vol. 11, No. 10, October, 2024, pp. 2859-2868
Journal homepage: http://iieta.org/journals/mmep

Investigating the Effects of Canard Dihedral Angle on the Wing Span Loading in a Forward-Swept Wing Aircraft at Transonic Speeds at Steady State Conditions Using Computational Fluid Dynamics

Ahmed Tawfeeq Mustafa Ali Abed*, Abdnoor Jameel Al-Hamadani, Mustafa Kamal Mustafa Al-Naser

Department of Aeronautical Engineering, College of Engineering, University of Baghdad, Baghdad 10071, Iraq

Corresponding Author Email: a.t.abed@coeng.uobaghdad.edu.iq

https://doi.org/10.18280/mmep.111029

Received: 26 June 2023
Revised: 7 October 2023
Accepted: 22 October 2023
Available online: 31 October 2024

Keywords:
aerodynamics, canard effect, CFD, forward swept wing, pressure distribution, shock wave, transonic, wing loading

ABSTRACT

Forward-swept wings were researched and introduced to improve maneuverability, control, and fuel efficiency while reducing drag and they are often used alongside canards, to further enhance their characteristics. In this research, the effects of canard dihedral angles on the wing loading of a forward-swept wing in transonic flow conditions were studied, as the wing loading provides a measure of wing's efficiency (lift/drag). A generic aircraft model from literatures was selected, simulated, and compared to, using CFD software ANSYS/Fluent where the flow equations were solved to calculate the aerodynamic characteristics. The research was carried at two different Mach numbers, 0.6 and 0.9, for five different canard dihedral angles which traverses from below the wing plane to above it, at various flow angles of attack. It was concluded that as the dihedral angle increased, lift increases for the same angle of attack for Mach 0.6 and 0.9 which increases the efficiency of the wing. The wing span loading occur at 10° dihedral angle for both Mach speeds, while, at 10° anhedral, the lift was minimal due to leading-edge flow separation on the FSW's lower surface. Thus, it is concluded that the canard at positive dihedral angles ensures increased wing span loading efficiency.

1. INTRODUCTION

The forward swept wing (FSW) concept, where wings face forward, emerged during World War II. These wings improve maneuverability, control, and fuel efficiency while reducing drag. They are often used alongside canards, which add lift, and stability features.

FSW-canard configuration allows excellent control in air combat at angles up to 45 degrees. These fighter planes are designed for supersonic capabilities, providing advantages like rapid engagement and high-altitude performance.

Previously, wing divergence issues prevented the full benefits of FSW. However, using advanced composite materials has helped overcome this problem through tailored wing structure based on the analysis of wing loading at different flying conditions [1].

Due to the complex and expensive requirements of any aircraft utilizing FSW, research on such configuration were limited due to its complicated flow phenomenon's [1] specifically in the transonic region with all its complicated characteristics [2]. With the advancement of material science, improved manufacturing techniques, and efficient electronic control systems FSW configuration witnessed increased interest by researchers in the past decade.

Mann and Mercer [3] used a transonic analysis method and design process to create the wing and canard of a forward-swept-wing fighter for excellent transonic maneuvering performance. Considering the strong induced-flow effects, this method calculates transonic flow over the combined canard, wing, and fuselage. The theory supported by extensive experimental measurements provided a good estimate of wing pressure during transonic maneuvers. A comparison with an FSW configuration showed equal trimmed drag at Mach 0.90 and a lift coefficient of 0.9. During transonic manoeuvres, the forward-swept-wing design had similar trimmed drag levels as the HiMAT and X-29 configurations.

Zhang et al. [4] researched the aerodynamic characteristics between the canard and wing of the canard-forward swept wing aircraft configurations numerically at low Reynolds numbers. A unique configuration of forward-swept canard was also investigated. CFD was applied via ANSYS/Fluent. The research concluded that at low angles of attack ($\alpha<10^{\circ}$), canard-FSW aerodynamics rely on canard geometry and relative positions to the wing. At high angles ($\alpha>20^{\circ}$), performance involves canard shape and vortex features like strength and location. Backwards-swept canards create secondary vortices more easily than forward-swept canards, providing more lift force.

Lei et al. [5] conducted a numerical study of the aerodynamic characteristics of FSW-tail aircraft at a Mach number of 1.5 with different wing positions was carried out. Spalart-Allmaras (S-A) turbulence model was used to account for the viscous effects. It concluded that the vertical position of FSW at a high angle of attack, lift, drag and center of

pressure coefficients decreases as the FSW moves downward relative to the tail position.

Xinbing et al. [6] studied the aerodynamic characteristics of variable forward-swept wing at subsonic flow conditions up to Mach 0.7 using CFD. The results showed that when flying at a low angle, the lift, drag, and moment coefficients increase with a higher forward-swept angle. However, at a high angle of attack, these coefficients decrease as the forward-swept angle increases.

Many studies utilized CFD and experimental investigation to determine complex aircraft geometry with high reliability of CFD results as in previous studies [7-13]. While it can be concluded from references [14-20] that use of different meshing techniques in conjunction with turbulent models is crucial in the accuracy of CFD results.

It can be seen that wing loading was not the focus of the aforementioned studies. In this work, a computational fluid dynamic analysis will be carried out to study the effects of a canard dihedral angle on the wing loading of a FSW in high subsonic and transonic flying conditions.

2. COMPUTATIONAL DOMAIN

2.1 Geometry

This research was carried out on a model which represents a highly maneuverable fighter configuration equipped with a forward-swept wing and canard [3]. Figure 1 shows the replication of this model.

Figure 1. Aircraft modelled in SolidWorks

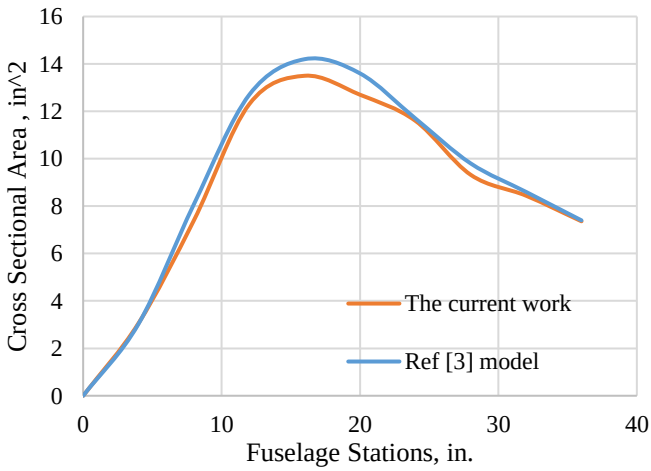

Figure 2. Cross-sectional area comparison chart

The aircraft model was drawn by SolidWorks based and compared to data provided by Mann and Mercer [3], the comparison in Figure 2, showed that the maximum error is 6.6% which is within acceptable limits.

2.2 Research methods

The current project examines the wing loading of the FSW when the dihedral angle of the canard is changed in the transonic region. The current research utilized simulation software (ANSYS/Fluent) to simulate the environment in which the aircraft will experience the same conditions due to its well-established reliability, accuracy, and versatility according to academic and industry standards.

2.3 Modelling

As stated previously, the model was drawn using SolidWorks. The enclosure was chosen to be a sphere where the radius of the sphere is 20 m which is more than 20 times the wing's main aerodynamic chord length as shown in Figure 3. The reason for that dimension is to effectively approximate true infinite-extent conditions, due to that, the far-field boundary should be placed sufficiently far from the object of interest [7]. Symmetry condition around the lateral-vertical axis of the aircraft was also applied to reduce computational cost and time. Figure 4 shows the different setups of the model.

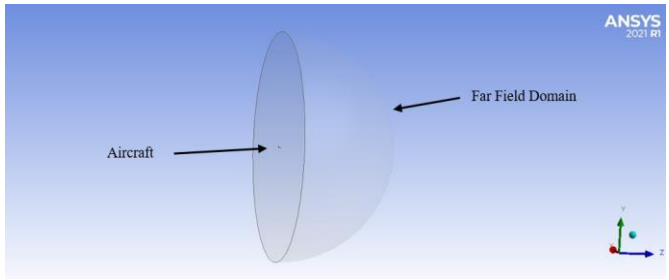

Figure 3. Semi-sphere used for the far field domain

Figure 4. Configurations of canard dihedral angles

2.4 Meshing

The mesh was chosen to be an unstructured mesh with tetrahedral elements distributed all over the domain where the software uses the Delaunay triangulation method for tetrahedral [7]. The primary focus is on concentrating the elements on the surface of interest, specifically the wing and canard, in order to optimize computational cost and time. This approach is necessitated by the limited availability of computational power.

To evaluate the current mesh quality, metrics such as Skewness and Orthogonality are used to measure the deviation

of cell shapes from ideal ones. The average skewness value obtained is 0.22, while the average orthogonal quality value is 0.78. Both average values fall within the excellent range of recommended values according to the ANSYS Fluent user guide [7].

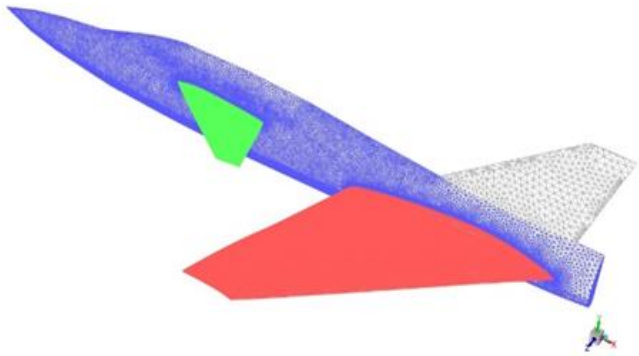

Figure 5. Aircraft meshing

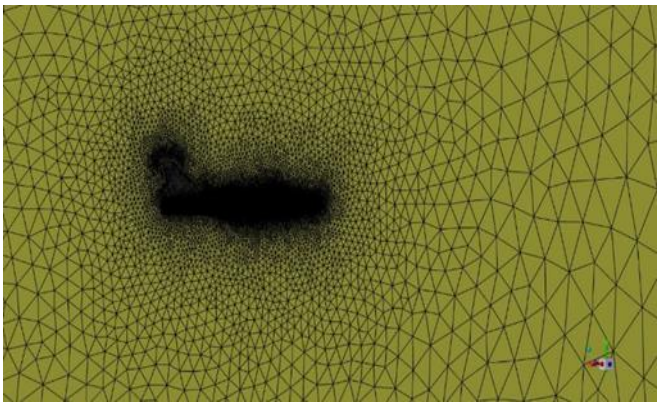

Figure 6. Aircraft meshing in the domain

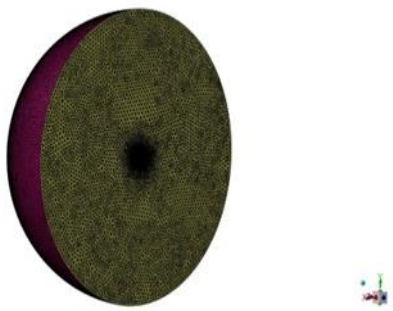

Figure 7. The meshing of the domain

Figure 5 and Figure 6 demonstrate that the mesh density is increased in areas requiring precise analysis. In Figure 7, the model cells were smaller compared to the domain meshing, emphasizing a concentrated focus on the model.

A growth rate of 1.1 were used to ensure smooth transition of the cells from the fine regions, such as the wing, to the coarse regions, such as the far field which maintains stability of the solution and accuracy of the results, also, capture proximity and capture curvature were activated to simulate all possible geometric features with sufficient mesh resolution at which this option is recommended by the reference [7].

Viscous effect was modelled using standard $(k-\varepsilon)$ as it represents the only viable model in terms of computational cost. This model can be implemented with $11.63 < y^{+} < 500$ [2]. The boundary layer is modelled using inflation layers to achieve the desirable y^{+} as shown in Figure 8 and Figure 9.

As can be seen in Figure 10, the values of y^{+} on the area of interest (wing and canard) for the final mesh are within limits.

⊞ Sizing	
⊞ Quality	
⊟ Inflation	
Use Automatic Inflation	Program Controlled
Inflation Option	First Layer Thickness
First Layer Height	1. mm
Maximum Layers	5
Growth Rate	1
Inflation Algorithm	Pre
View Advanced Options	No

Figure 8. Inflation layers settings used in the meshing

Figure 9. Main wing inflation layer

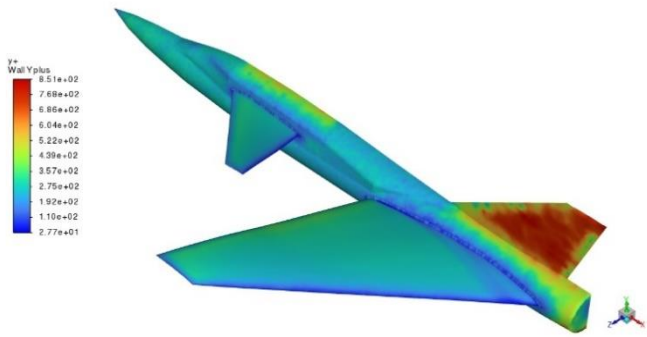

Figure 10. Values of y^{+} in the area of interest

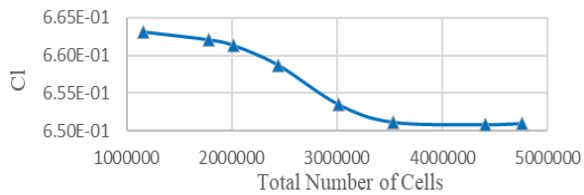

Figure 11. Change of lift coefficient with the grid size

To evaluate grid independence, save computation time and gain better accuracy, a grid independence study is conducted by considering C_l as a parameter for comparison. Grid independence study is crucial for evaluation accuracy and determining optimal mesh resolution. It plays a significant role in obtaining reliable and accurate results. Figure 11 shows a mesh independence study conducted at Mach 0.6 and an angle of attack 6.2°. It can be seen that when the number of elements

increased, the value of C_l comes to settle at 0.65118 with a number of elements of 3,535,565. The curve shows that the differences between the last two values for the coefficient of lift are negligible, around 2.46×10^{-4}, thus the number of cells used for all cases is 4.75 million.

2.5 Methods of solutions

A steady-state approach was employed in conjunction with a pressure-based solution strategy. The ideal gas law was utilized, and the Sutherland viscosity equation was selected to account for gas viscosity. Additionally, the energy equation was enabled to capture thermal effects. To enhance the accuracy of predicting free shear layers at high Mach numbers, the compressibility effect was activated. The solution procedure involved a Pressure-Velocity coupled scheme, wherein the governing equations were formulated as second-order equations. Pseudo-transient and high-order term relaxation techniques were utilized to facilitate convergence and improve the stability of the solution. Hybrid initialization, is employed in the calculation step.

2.6 Boundary conditions

It was recommended by reference [7] to use pressure far field boundary condition when dealing with variable density, compressible, flow. Also, it provides an efficient method for changing the flow incidence angles without the need to regenerate the mesh, thus, the pressure far field was chosen to be the boundary condition for the domain in which the values of Mach numbers and specific angles of attack were the inputs. Symmetry condition was also used to reduce the time of computation and the aircraft was considered as a stationary wall with no-slip condition.

2.7 Validation and verification

For validation, a comparative test was carried out with the experimental data presented by Mann and Mercer [3]. The comparison was carried out at two different Mach numbers, 0.6 and 0.9. The results showed a good agreement indicating that the flow conditions were simulated accurately. In Mach 0.6, the angle of attack started from 0.6° and increased till reached 8.2° in which Cl was almost the same with reference [3] data at the small angles of attack and started to deviate as the angle increased as shown in Figure 12, but still within the acceptable range of error, as maximum error was 15.27%.

This increased value of error at higher angles of attack is due to limited computational resources that restricted the simulation of the flow exactly when the fluid experiences a large portion of turbulent flow. Essentially, Versteeg and Malalasekera [2] stated that the $k-\varepsilon$ model fails to accurately capture the complex flow characteristics near curved surfaces, resulting in an inaccurate representation of shear stress and an inadequate prediction of separation phenomena. This limitation affects the accuracy of the solution and tend to simulate early separation of the flow which means underestimation of lift coefficient and overestimation for drag coefficient. Due to the limitations of the computational power the values of y^+ of unity or less cannot be achieved, thus $k-\varepsilon$ model is the only viable model for the current project. Nonetheless, this issue is expected to be addressed in forthcoming research. The drag polar also has been checked for the present case compared with experimental data from the study conducted by Mann and Mercer [3], it shows the same trend. The primary objective of this research is to comprehensively capture the flow characteristics across the entire area of interest as shown in Figure 13.

The same can be seen at M0.9 with the same output results. The mass imbalance was also evaluated as shown in Figure 14 and it was noted that it reached zero value in most regions of the domain which means the inlet flow is the same flow that goes out without any loss or leakage of the flow in the domain.

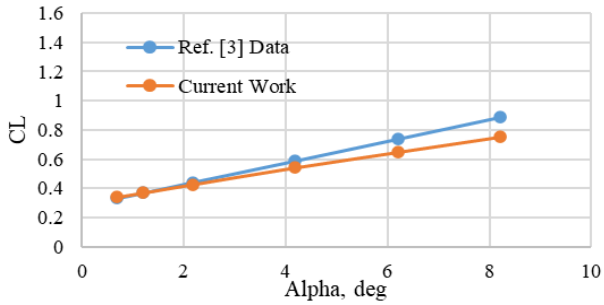

Figure 12. Comparison of Cl between current work with reference [3]

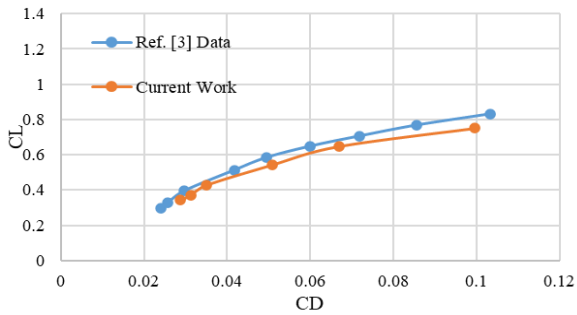

Figure 13. Comparison of drag polar at AOA 6.2 and M0.6 of current work vs. data from reference [3]

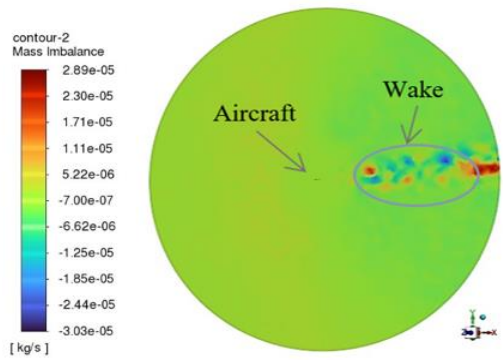

Figure 14. Mass imbalance across the domain at AOA 6.2 and M0.6

3. RESULTS AND DISCUSSION

After the validation and verification step has been accomplished, the examination of the effect of the canard dihedral angles on the wing loading has been carried out at two different Mach numbers, 0.6 and 0.9, at different angles of attack and multiple canard dihedral angles. In total 55 cases were simulated and analyzed.

3.1 Results at Mach 0.6

Figure 15 displays the variation of lift coefficient with changing canard dihedral/anhedral angles at Mach 0.6 and an angle of attack of 6.2˚. It shows that altering the canard's dihedral angle affects the lift generated by the aircraft, although the specific values of the lift coefficient differ slightly. Despite these variations, the overall trend of the lift coefficient remains consistent. The anhedral canard angles produce the lowest lift coefficient, whilst the dihedral canard angles produce the highest lift coefficient. This is due to the effect of canard downwash, which decreases the effective angle of attack on the onboard section of the wing and increases it on the outboard section, thus delaying the separation of the flow and redistributing the pressure and increasing wing efficiency. This effect is more apparent when the canard has a dihedral angle, as shown in Figure 16, Which shows the wing loading of a FSW at Mach 0.6 and AOA 6.2˚ under the influence of different dihedral/anhedral canard angles, where the lift varies along the span of the wing and it exhibits changes in the lift distribution caused by the presence of the canard. It can be seen that the wing loading trend is the same but with different values at different canard angles. It's clearly seen that the canard with a dihedral of 10˚ has the highest influence on the lift at the main wing root while the lowest lift at the main wing tip. This is due to the effect of the generated downwash by the canard on the onboard region of the main wing to experience higher effective AOA which means more lift compared to regions that experienced lower effective AOA. The pressure distribution over the wing confirms this behavior as seen in Figure 17.

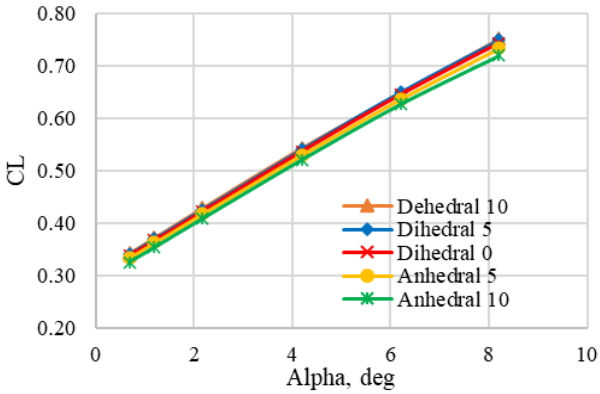

Figure 15. Variation of lift coefficient vs. AOA at M0.6 with different canard's dihedral angles

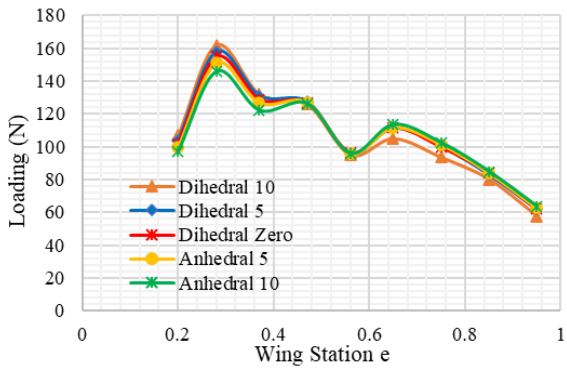

Figure 16. Wing loading of FSW under the influence of different canard dihedral angles at AOA 6.2˚, M0.6

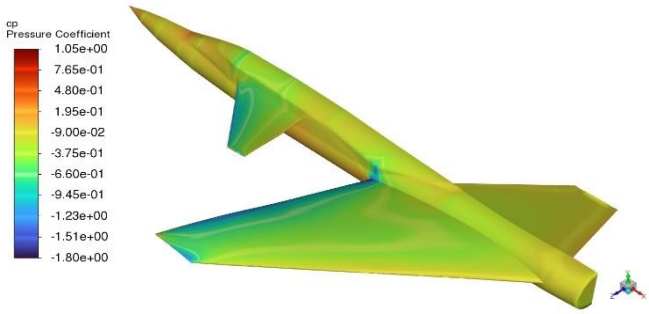

Figure 17. Pressure contours at AOA 6.2˚, M0.6˚

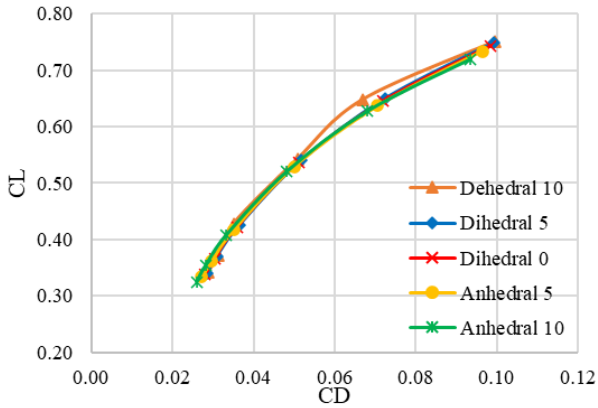

Figure 18. Drag polar at M0.6˚ for different canard dihedral angles

The drag polar for different canard dihedral angles is drawn in Figure 18, from which it can be concluded that as the dihedral increases the lift and the drag both increase, this is due to the increased local angle of attack which leads to increased lift and increased induced drag.

Figure 19 illustrates the path lines in which the flow rolls up from the vortices of the canard which illustrate the modification of the effective AOA caused by the downwash is more significant near the canard and becomes less pronounced towards the wingtips.

While at canard anhedral 10˚ the opposite influence on the main wing can be seen in Figure 20 which means higher lift at the main wing tip and lower lift at the main wing root compared to other canard dihedral/anhedral angles. In the canard of anhedral 10˚, with a downward-angled canard, the lift generated by the canard will be greater towards the wingtips and lower towards the center section.

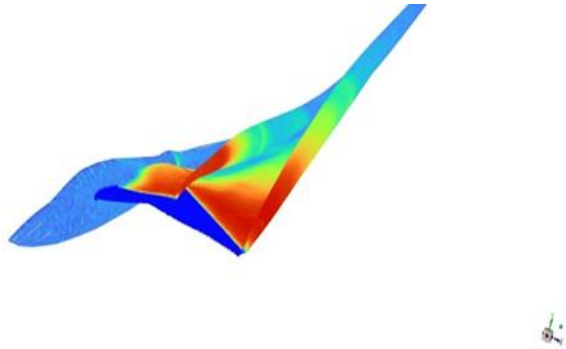

Figure 19. Particle path lines at M0.6 and AOA 6.2˚ canard dihedral 10˚

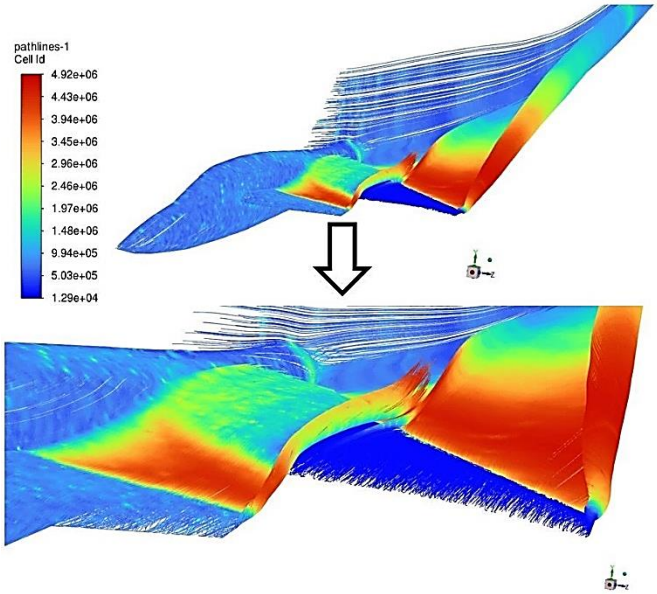

Figure 20. Particle path lines at M0.6 and AOA 6.2˚ canard anhedral 10˚

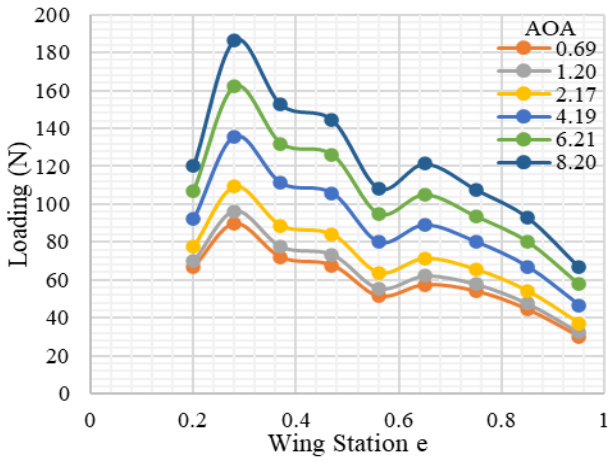

Figure 21. Wing loading of FSW at different angles of attack and M0.6 for canard anhedral 10˚

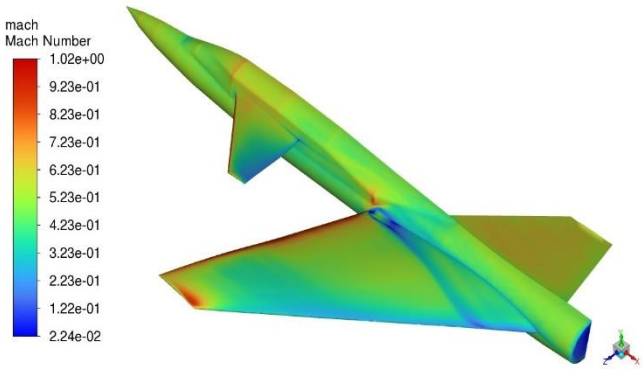

Figure 22. Mach contours at dihedral 10˚, AOA 8.2˚ and M0.6

This can lead to a more tapered lift distribution as shown in Figure 21, which can improve roll stability and reduce the likelihood of tip stall.

In Figure 22, Mach contours for the canard at 10˚ dihedral angle and AOA 8.2˚ shows shock waves formations at the leading edge of both the FSW and the canard, also a noticeable shock at the wing tip.

The most important phenomenon that have been captured in is the flow separation at the wing root which is also clearly seen in Figure 23. This wing root separation is one of the unique characteristics of the FSW [3], however, due to the viscous model used in the present work it will be one of the sources of the deviation between the computational results of this work and the experimental measurements [3]. These results are crucial in the determination of the aircraft performance, stability, and control during cruise flight and the early stages of dogfighting maneuvers, also used as input in the structural design of the wing.

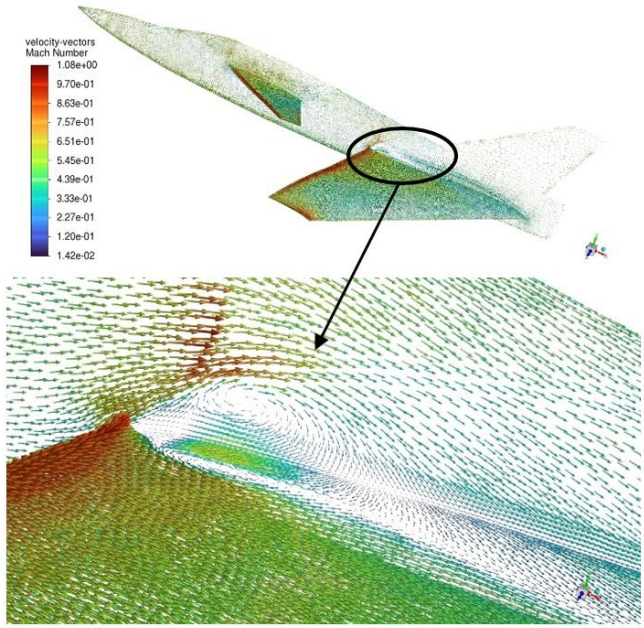

Figure 23. Flow separation at the wing root leading edge

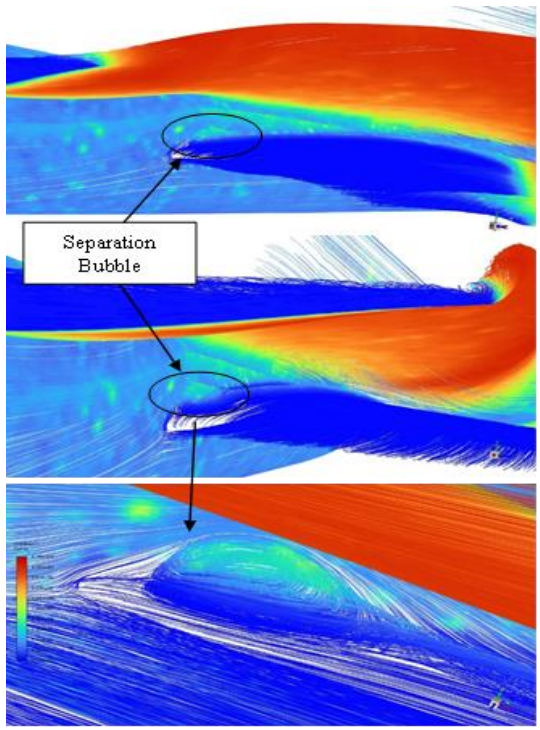

Figure 24. Effect of flow separation on wing camber at the root leading edge

It is noted that FSW root separation did not affect the generation of lift at the inboard section of the wing due to the fact that the separation is enclosed in a separation bubble rather than separated freely, this will cause the flow to behave as if it moves over a newly formed thicker wing with a larger camber as shown in Figure 24.

3.2 Results at Mach 0.9

At Mach 0.9 free stream flow velocity the computational results show the impact of shock waves and the effect of changing canard dihedral angles on the FSW more clearly as compared to that at Mach 0.6. This is due to the fact that the effects of transonic flow are more formidable. In Figure 25, the wing loading of FSW at M0.9 and AOA of 6.2˚, Shows almost the same output results of M0.6 except the values of the lift generated on the main wing are much higher compared to the lift generated at M0.6, and this is due to higher local velocity and higher suction pressure. It is to be noted that the compressibility effect became more significant at M0.9, it is an indicator that the shockwaves did not encounter any decreases in the lift generated. It can be seen that the canard dihedral effect of 10˚ causes the lift to be higher on the wing root and the lowest on the wing tip compared to other canard's dihedral angles which is a result of the downwash generated from the canard on the onboard section of the wing and delay the separation while the canard upwash increases the effective AOA at the outboard section of the wing, again redistributing the lift and increases the wing effectiveness.

These results and conclusions agree well with Figure 26, which shows that at the anhedral angle of 10˚, the model will generate the lowest lift compared to other canard's dihedral angles. The canard's impact on the overall lift is significant, not only influencing the main wing but also leading to enhanced wing efficiency and reduced drag characteristics.

The drag polar behavior is similar to that at M0.6 as shown in Figure 27, where the dihedral increases the lift and the drag, this is due to the increased local angle of attack which leads to increased lift and increased induced drag.

This can be confirmed with the data from Figure 28, where the shockwaves formed on the FSW as the flow accelerates from the subsonic flow between the canard and the FSW to supersonic flow over the upper surface of the FSW due to the local geometry. The velocity of the flow exhibits a progressive increase until it reaches critical conditions, leading to the formation of a weak shockwave. Subsequently, the flow undergoes an expansion accompanied by the formation of a strong shockwave, resulting in a transition of the flow to a subsonic state. This behavior is well known in transonic flow as the Lambda shockwave [3]. In Figure 29, the coefficient of pressure increases significantly after the shock regions, this area of pressure indicates that the shock waves are strong which implies a significant compression to the airflow. Regions of high pressure after the shock wave cover an area that is close to the wing trailing edge, which means a small region that has a boundary-layer flow separation; accordingly, this area will affect the computation of aerodynamic forces such as lift and drag.

In Figure 30, it is clearly seen that the canard tip vortex influences directly the flow over the main wing surface affecting the lift generated by the wing. This canard dihedral angle produces the optimum lift value compared to other dihedral angles.

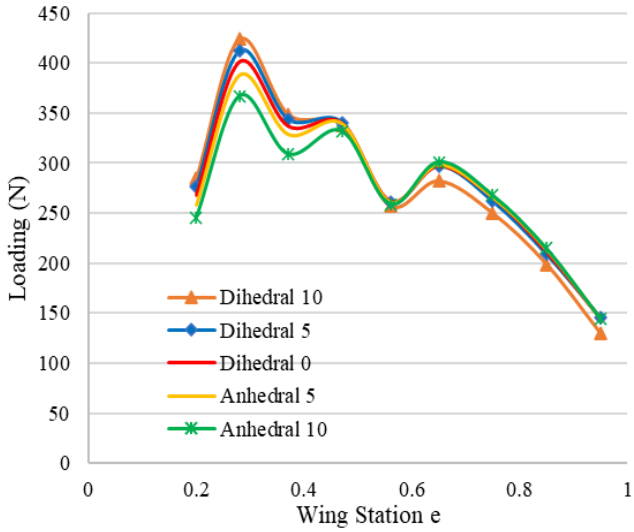

Figure 25. Wing loading at M0.9˚ and AOA of 6.3˚ for different canard dihedral angles

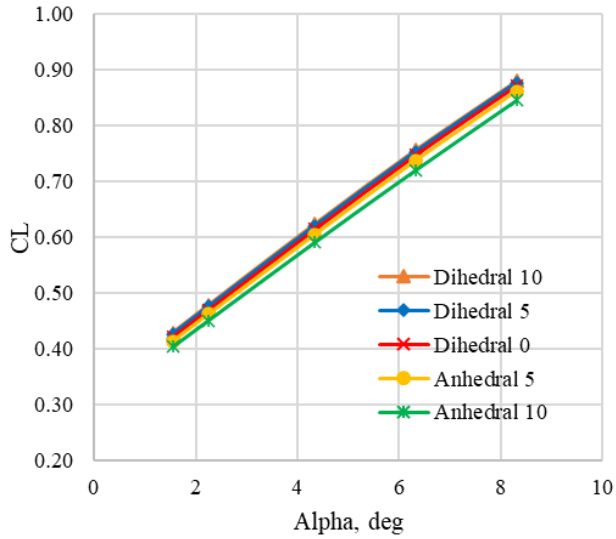

Figure 26. Variation of lift coefficient with AOA at M0.9 for different canard dihedral angles

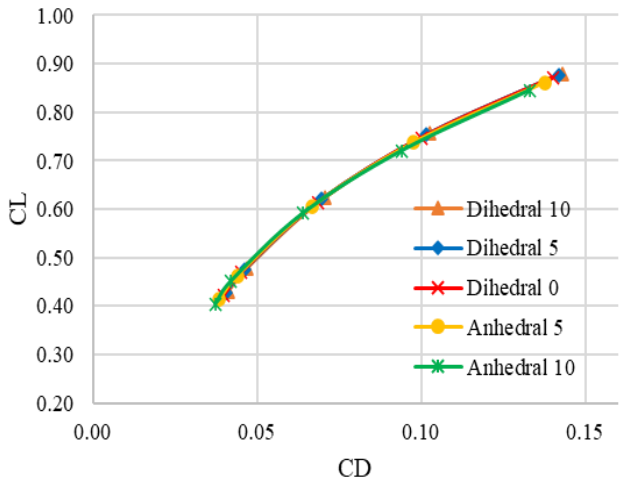

Figure 27. Drag polar at M0.9 for different canard dihedral angles

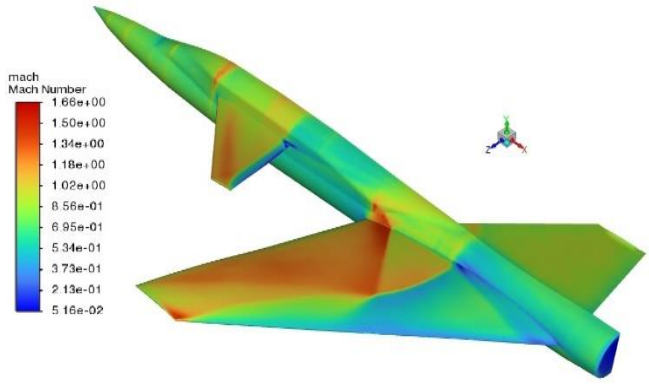

Figure 28. Mach contours at dihedral of 10˚ and AOA of 6.3˚

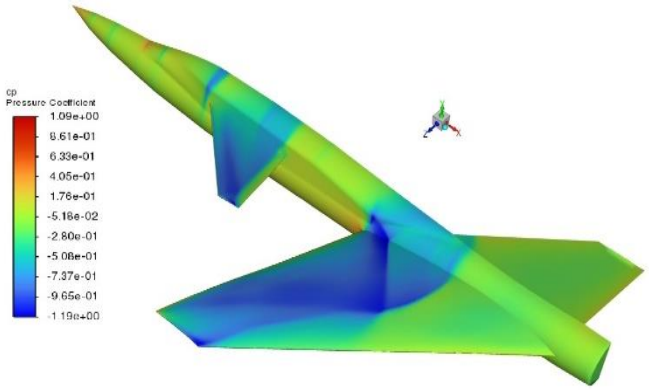

Figure 29. Pressure coefficient contours at dihedral of 10˚ and AOA of 6.3˚

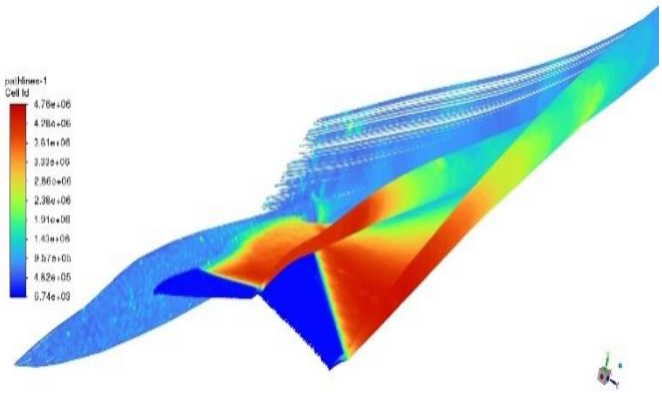

Figure 30. Particle path lines at dihedral of 10˚ and AOA of 6.3˚

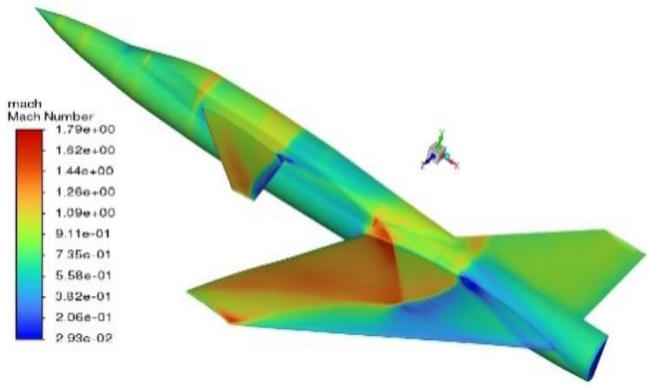

Figure 31. Mach contours at dihedral of 10˚ and AOA of 8.3˚

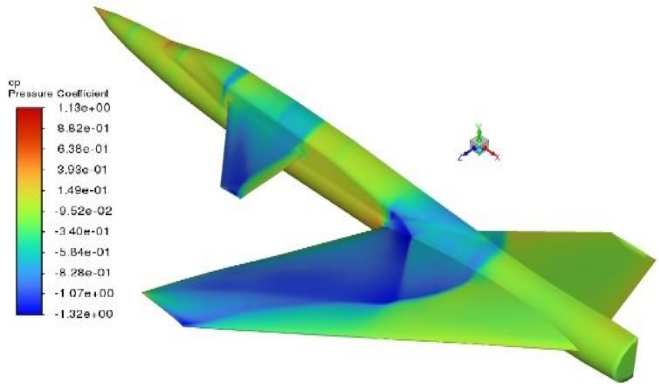

Figure 32. Pressure coefficient contours at dihedral of 10˚ and AOA of 8.3˚

The above-explained flow behavior was noticed in most cases with a few remarkable interesting phenomena that need to be emphasized. As the AOA increases to 8.3˚, the lambda shock wave becomes stronger especially at the root of the FSW as shown in Figure 31. It can be seen at this high angle there are two separated flow regions, the first at the trailing edge of the canard, and the second near the middle section of the FSW root. Both are the result of strong shockwaves formed near these locations, which can also be confirmed in the pressure coefficient contours in Figure 32 as the pressure increases after the shockwaves.

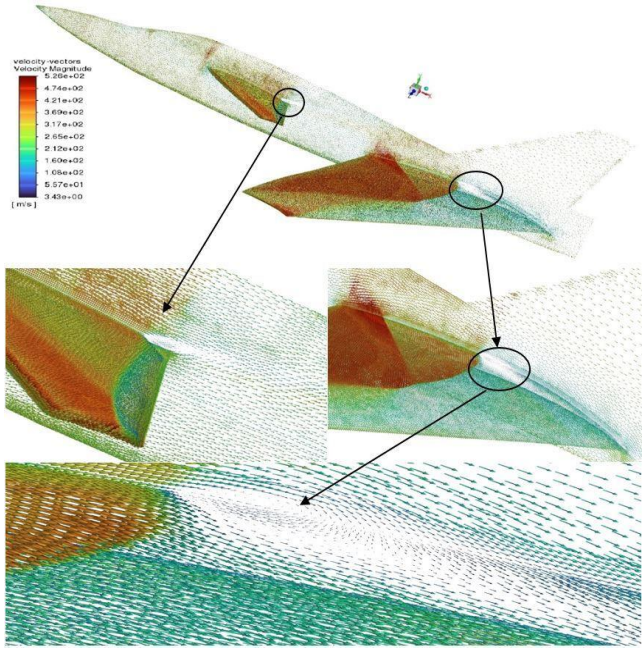

Figure 33. Velocity vectors at dihedral of 10˚ and AOA of 8.3˚ showing regions of separated flow on the canard and the FSW due to shock wave-boundary layer interaction

The separation has occurred due to shock wave-boundary layer interaction, which is a phenomenon outside the scope of this research and will be addressed in details in further study to analyze its effects on aerodynamic characteristics, prediction of its strength, and location to enhance the design of FSW aircraft. This affirms that the suggested methods used in the present work were able to capture such complex compressible-viscous phenomena with acceptable accuracy. Due to the high velocity and the design of the model and the characteristics of the FSW, both separated regions formed a

separation bubble which prevented any drop in the lift generation as can be seen in Figure 33, but caused an increased drag as indicated in Figure 27 before.

Figure 34. Velocity vectors at anhedral of 5° and AOA of 1.55° showing separated flow on the lower surface of the FSW

At a canard anhedral angle of 5°, the flow experience separation but on the lower surface of the FSW, as shown in Figure 34. This separation is due to the rapid change of the flow direction on the lower surface at the leading edge of the FSW and the interaction of the canard tip vortices with the flow over the FSW which can be seen in Figure 35. This separation occurs at a low AOA of 1.55° and decreases as the AOA increases until AOA 6.3° the flow is completely attached to the lower surface as can be seen in Figure 36. The same effect was observed at canard anhedral 10° as in Figure 37. The effect of such separation explains the noticeable reduction in lift for those two cases which was indicated in Figure 27 before. The results show that flow over FSW remains attached effectively and wing won't stall in the transonic region. These results used to determine the size and optimum location of control surfaces which affects aircraft control.

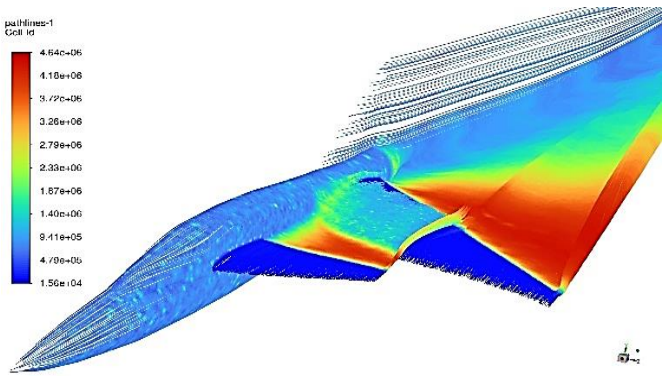

(a) Velocity path lines over the main wing

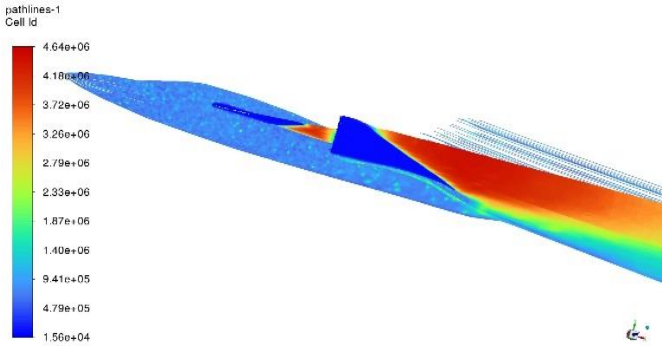

(b) Interaction of canard vortex with the main wing

Figure 35. Particle path lines at anhedral of 5° and AOA of 1.55° showing flow interaction between canard and FSW

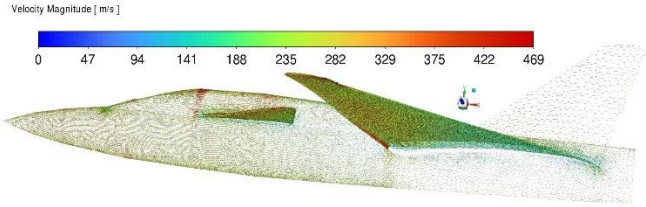

(a) AOA 2.25°

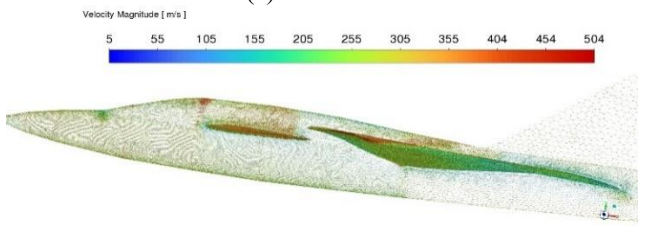

(b) AOA 6.3°

Figure 36. Velocity vectors at anhedral of 5° and AOA of 2.25° and 6.3°

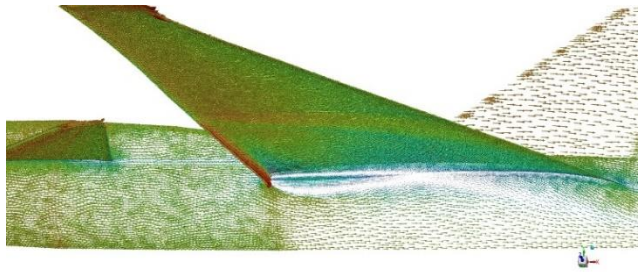

(a) AOA 1.55°

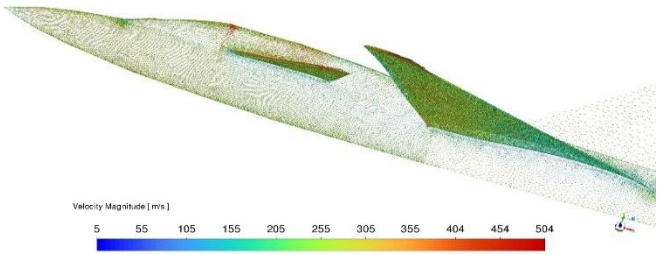

(b) AOA 6.3°

Figure 37. Velocity vectors at anhedral of 10° and AOA of 1.55°, and 6.3° showing the decreasing region of the separated flow on the lower surface of the FSW

4. CONCLUSIONS

This research investigated the wing loading for FSW under the influence of a canard at five different dihedral angles in transonic flow conditions at two different Mach numbers. The aircraft model was based on data from reference [3]. CFD was applied via Fluent program to estimate the aerodynamic characteristics. The mesh was optimized under many limitations to full fill the physical and numerical requirements. The solution methods were validated with experimental data from reference [3]. The findings indicate that:

- The lift increases as the dihedral angle increases at the same angles of attack for both Mach numbers, 0.6 and 0.9.
- At the transonic regime, the formation of lambda shock wave caused an increase of drag due to flow separation

as the result of the boundary layer shock wave interaction.

- The highest lift and the best wing span loading were at the dihedral angle of 10° for both Mach numbers, which provides the highest aerodynamic efficiency.
- At anhedral 10° the aircraft has the lowest lift due to the leading-edge flow separation on the lower surface of the FSW, which offers the least aerodynamic efficiency.

The aerodynamic characteristics of FSW in transonic conditions can be investigated using different turbulence models and finer mesh to simulate the flow separation accurately and increase solution accuracy. Also, an investigation is suggested to be carried out based on detached eddy simulation to better simulate the flow separation captured in the current research as it is time dependent phenomena. The understanding of the span loading provided by this study is crucial to design the wing aerodynamically and structurally.

REFERENCES

[1] Johnsen, F.A. (2013). Sweeping forward: Developing & flight testing the Grumman X-29A forward swept wing research aircraft. National Aeronautics and Space Administration.

[2] Versteeg, H.K., Malalasekera, W. (2007). An Introduction to Computational Fluid Dynamics: The Finite Volume Method. Pearson Education.

[3] Mann, M.J., Mercer, C.E. (1986). Forward-swept wing configuration designed for high maneuverability by use of a transonic computational method. No.: NASA-TP-2628.

[4] Zhang, G.Q., Yu, S.C.M., Chien, A., Yang, S.X. (2013). Aerodynamic characteristics of canard-forward swept wing aircraft configurations. Journal of Aircraft, 50(2): 378-387. https://doi.org/10.2514/1.C031740

[5] Lei, J., Zhao, S., Wang, S. (2016). Numerical study of aerodynamic characteristics of FSW aircraft with different wing positions under supersonic condition. Chinese Journal of Aeronautics, 29(4): 914-923. https://doi.org/10.1016/j.cja.2016.06.006

[6] Xinbing, S.U., Wen, J., Xiwei, Z., Junyi, Z. (2020). Research on aerodynamic characteristics of forward-swept wing with inclined basic airfoil. Journal of Physics: Conference Series, 1605(1): 012075. http://doi.org/10.1088/1742-6596/1605/1/012075

[7] Fluent ANSYS. (2011). ANSYS Fluent User's Guide. ANSYS Inc. Release 17.2.

[8] Ali, A.H. (2017). Aerodynamic characteristics of a rectangular wing using non-linearvortex ring method. Journal of Engineering, 23(4): 125-141. https://doi.org/10.31026/j.eng.2017.04.08

[9] Abd, D.A., Ali, A.H. (2020). Aerodynamic characteristics comparison between spiroid and blended winglets. Journal of Engineering, 26(4): 33-46. https://doi.org/10.31026/j.eng.2020.04.03

[10] Zhao, X.W., Su, X.B., Jiang, W., Zhang, J.Y. (2020). Simulation research on the influence of basic airfoil oblique angle on the aerodynamic characteristics of forward swept airfoil. In 2020 6th International Conference on Mechanical Engineering and Automation Science (ICMEAS), Moscow, Russia, pp. 135-139. https://doi.org/10.1109/ICMEAS51739.2020.00033

[11] Wibowo, S.B., Basuki, B., Sutrisno, Rohmat, T.A., Siswantoro, S., Nugroho, F., Ginting, P., Anwar, Z. (2021). Vortex dynamics study and flow visualization on aircraft model with different canard configurations. Fluids, 6(4): 144. https://doi.org/10.3390/fluids6040144

[12] Mousa, N.A., Attia, O.H., Mahmood, H.A., Adam, N.M. (2022). Optimization efficiency of the aircraft wing of Cessna 172 Skyhawk by absorbent adverse pressure using tangential suction slot without vacuum device. Mathematical Modelling of Engineering Problems, 9(3): 731-738. https://doi.org/10.18280/mmep.090320

[13] Naeem S.M. (2024). Structural and stress analysis of NACA0012 wing using SolidWorks. Mathematical Modelling of Engineering Problems, 11(8): 2181-2186. https://doi.org/10.18280/mmep.110820

[14] Dong, Y.Z., Shi, Z.W., Chen, K., Chen, J. (2019). Experimental investigation of the effects of sideslip on canard-configuration aircraft at high angle of attack. AIP Advances, 9(5). https://doi.org/10.1063/1.5093559

[15] Kanazaki, M., Setoguchi, N. (2023). Characteristics of vortices around forward swept wing at low speeds/high angles of attack. Aerospace, 10(9): 790. https://doi.org/10.3390/aerospace10090790

[16] Hami, K. (2021). Turbulence modeling a review for different used methods. International Journal of Heat and Technology, 39(1): 227-234. https://doi.org/10.18280/ijht.390125

[17] Setoguchi, N., Kanazaki, M. (2020). Low-speed and high angle of attack aerodynamic characteristics of supersonic business jet with forward swept wing. In AIAA Scitech 2020 Forum, Orlando, USA, p. 534. https://doi.org/10.2514/6.2020-0534

[18] Su, X.B., Jiang, W., Zhao, X.W. (2019). Study on the influence of swept angle on the aerodynamic characteristics of the cross-section airfoil of a variable swept-wing aircraft. IOP Conference Series: Materials Science and Engineering, 685(1): 012016. https://doi.org/10.1088/1757-899X/685/1/012016

[19] Hajipour, A., Lavasani, A.M., Yazdi, M.E. (2021). Investigation of wall function effects on aerodynamic characteristics of turbulent flow around a simplified high-speed train. International Journal of Heat and Technology, 39(1): 309-318. https://doi.org/10.18280/ijht.390134

[20] Zhang, J.Y., Su, X.B., Jiang, W., Zhao, X.W. (2021). Influence of basic airfoil layout on aerodynamic characteristics of forward-swept wing. IOP Conference Series: Materials Science and Engineering, 1102(1): 012004. https://doi.org/10.1088/1757-899X/1102/1/012004

NOMENCLATURE

AOA	angle of attack, degree
Cd	drag coefficient, dimensionless
CFD	computational fluid dynamics
Cl	lift coefficient, dimensionless
Cp	pressure coefficient, dimensionless
FSW	forward swept wing
HiMAT	high maneuverable aircraft technology
LE	leading edge
M	Mach number
TE	trailing edge